

In-situ Growth of Carbon Nanosheets Intercalated with TiO₂ for Improving Electrochemical Performance and Stability of Lithium-ion Batteries^①

HU Yan-Jie^{a, b, c} YIN Yan-Hong^{a②} ZHANG Ming^{b, c}
WU Zi-Ping^{a②} SHEN Zhong-Rong^{b, c②}

^a (Faculty of Materials Metallurgy and Chemistry,

Jiangxi University of Science and Technology, Ganzhou 341000, China)

^b (CAS Key Laboratory of Design and Assembly of Functional Nanostructures,
and Fujian Key Laboratory of Nanomaterials, Fujian Institute of Research on the
Structure of Matter, Chinese Academy of Sciences, Fuzhou 350002, China)

^c (The Laboratory of Rare-earth Functional Materials and Green Energy, Xiamen Institute of Rare
Earth Materials, Haixi Institute, Chinese Academy of Sciences, Xiamen 361021, China)

ABSTRACT *In situ* growth of carbon nanomaterials on active substance is a very favorable strategy for the preparation of electrode in lithium-ion batteries with excellent electrochemical performance and high stability. Small-sized TiO₂ nanoparticles intercalated into carbon nanosheets (CNS@TiO₂SNP-600) were successfully synthesized via *in-situ* polymerization-carbonization method, utilizing layered H₂Ti₄O₉ (HTO) as template and benzidine as carbon source. The morphology and size of TiO₂ are greatly influenced by carbonization temperature. The coin cell with the CNS@TiO₂SNP-600 electrode demonstrates a discharge specific capacity of 430.4 mAh·g⁻¹ at a current density of 0.1 A·g⁻¹, and the capacity retention rate is 88.1% after 100 cycles; and it also displays a high discharge specific capacity of 101.8 mAh·g⁻¹ at a high current density of 12.8 A·g⁻¹. The excellent electrochemical performances can be ascribed to the capacitance effect originated from the intercalated structure of *in-situ* grown CNS and TiO₂ nanoparticles. We believe this type of materials can be widely used in the lithium-ion batteries and other related green chemical fields.

Keywords: carbon nanosheets, TiO₂, *in situ* growth, template, storage lithium;

DOI: 10.14102/j.cnki.0254-5861.2011-3189

1 INTRODUCTION

Titanium dioxide (TiO₂) has been widely investigated as an electrode material for lithium-ion batteries due to its safety, rich resources, and high theoretical specific capacity. But its low electronic conductivity leads to the poor rate performance and low cycle stability, and further limits its wide application^[1]. To improve the lithium storage capability, rate performance, and cycle stability, the porosity of TiO₂ is usually increased to alleviate the volume expansion, and the

crystal particle size is reduced to improve the cycle stability^[2]. However, the most efficient strategy is to combine TiO₂ with carbon nanomaterials for increasing their contact area and conductivity, such as combining TiO₂ with carbon nanofibers by electrospinning, vapor deposition^[3-5], *in-situ* growth of TiO₂ on carbon nanotubes^[6, 7], intercalation of TiO₂ in the interlayers of graphene^[8-16] and so on. Based on the above strategies, the conductivity of TiO₂-based materials can be enhanced, and thus the rate performance and cycle stability performance can be further improved. Nevertheless, the high

Received 22 March 2021; accepted 6 May 2021

① This project was supported by the National Natural Science Foundation of China (22062008), the China Scholarship Council (201908360233), and the Jiangxi Provincial Department of Science and Technology (GJJ190436, 2019KY56)

② Corresponding authors. Yin Yan-Hong, E-mail: yinyanhong@jxust.edu.cn;

Wu Zi-Ping, E-mail: wuziping724@jxust.edu.cn; Shen Zhong-Rong, E-mail: z-shen@fjirm.ac.cn

length-width ratio and hydrophobic surface of carbon nanotubes inevitably limit their homogeneous dispersion, further inhibiting uniform distribution of TiO₂ nanoparticles. Meanwhile, the reported carrier function of graphene is not satisfactory, and the main reason is the fact that the interaction force between graphene and TiO₂ nanoparticles is weak, which is mainly ascribed to less functional groups in its plane except at the edge part. Therefore, it is vital to develop a more efficient route to synthesize carbon nanomaterials integrated with TiO₂ nanoparticles.

Recently, our group prepared a layered composite material combined with carbon nanosheets and TiO₂ layers by using amines as carbon source, through a procedure of intercalation, polymerization, and carbonization^[17-19]. This composite exhibits a much higher theoretical capacity compared to TiO₂, which is ascribed to the synergistic effect of ion insertion (conversion reaction) and interfacial capacitance effect (electric double layer effect)^[20, 21]. In our previous work, Ni element was introduced to control the shape of layered TiO₂. However, it would be removed by wet etching after carbonization process. The preparation procedure is complicated, eventually resulting in some oxygen vacancies existing in the TiO₂ lattice.

In order to simplify the preparation process, herein, a strategy for in-situ growth of carbon nanosheets (CNS) was performed by using benzidine as carbon source. Based on the ability of benzylamine to increase the interlayer distance of HTO, the benzidine can be easily embedded between the interlayers of HTO by replacing benzylamine through an exchange reaction. The in-situ grown CNS can effectively improve the conductivity of TiO₂. The morphology and size of TiO₂ can be mediated through controlling carbonization temperatures. The obtained CNS@TiO₂SNP-600 displays excellent electrochemical performance and high cycle stability, which is mainly due to the intercalated structure of CNS and TiO₂. We believe this type of materials can be widely used in lithium-ion batteries and other related green chemical applications.

2 EXPERIMENTAL

2.1 Materials

Benzylamine (C₇H₉N, 98.5%, Sinopharm Chemical Reagent Co., Ltd), benzidine (C₁₂H₁₂N₂, 99.5%, Yuanhang Reagent, China) and potassium carbonate (K₂CO₃, 99.0%, Sinopharm Chemical Reagent Co., Ltd). K₂CO₃ was placed in an oven at

120 °C for 24 hours to remove moisture before the experiment.

2.2 Synthesis of the material

HTO was firstly synthesized according to the method reported by Sasaki and his colleagues^[22], and its morphology is displayed in Fig. S1. Then, the poly-benzidine/TiO₂ sample was obtained through the process of intercalation, oxidative, and polymerization of benzidine by using HTO as template^[18]. Finally, the poly-benzidine/TiO₂ nanosheet was carbonized at 500, 600, and 700 °C in a reducing atmosphere (H₂/N₂ = 1/9 in V/V). Carbon nanosheets@TiO₂ nanosheets (CNS@TiO₂NS-500), carbon nanosheets@TiO₂ small-sized nanoparticles (CNS@TiO₂SNP-600), and carbon nanosheets@TiO₂ large-sized nanoparticles (CNS@TiO₂LNP-700) were obtained under different carbonization temperature of 500, 600, and 700 °C (Fig. 1), respectively.

In order to further characterize the physical properties of carbon nanosheets coated on TiO₂, TiO₂ was removed from the CNS@TiO₂NS-500, CNS@TiO₂SNP-600, and CNS@TiO₂LNP-700. In a typical experiment, 1.0 g of CNS@TiO₂NS-500, CNS@TiO₂SNP-600, and CNS@TiO₂LNP-700 was soaked in 25 mL 10 wt% HF aqueous solution, with the hydrothermal reaction kept at 100 °C for 12 h. Then, the reaction system was cooled down to room temperature, filtered, washed with deionized water and ethanol for several times. After drying at 60 °C overnight, the corresponding CNS products at different temperature are labeled as CNS-500, CNS-600, and CNS-700, respectively.

2.3 Materials characterization

The composition of all samples was analyzed by X-ray diffraction (XRD) spectra, using a Rigaku MiniFlex 600 diffractometer with CuK α irradiation. The chemical structure and properties of the samples were characterized by Fourier Transform Infrared Spectrometer (FTIR, Thermo Nicolet is 50, USA), Raman spectra (Lab RAM Aramis spectrometer, 532 nm laser), Scanning Electron Microscope (SEM, Zeiss Sigma 500), and Transmission Electron Microscope (TEM, FEI Talos 200s microscope equipped with a high-precision EDX spectroscopy detector). Thermogravimetric Analysis (TGA, Mettler-Toledo TGA System) was performed at 5 °C·min⁻¹ from 30 to 800 °C in oxygen atmosphere.

2.4 Electrochemical characterization

Galvanostatic charge/discharge cycling tests were conducted on a Neware battery cycler (Neware, Shenzhen) within a cut-off voltage window between 0.05 and 3.0 V. Cyclic Voltammetry (CV) behaviors of the cells were

conducted on a 760E electrochemical workstation (Chenhua, Shanghai) with a scan rate between 0.1 and 1 $\text{mV}\cdot\text{s}^{-1}$ in the voltage range of 0.05 ~ 3.0 V. Working-electrodes were prepared from 80 wt% activate material, 10 wt% valcun carbon XC-72 (Cabot, USA) and 10 wt% polyvinylidene fluoride (PVDF, HSV900, Kejing). The electrode slurry was coated on a copper foil (with doctor blade to control thickness) and dried overnight at 110 $^{\circ}\text{C}$ under vacuum. Standard CR2032-type coin cells were used to conduct electrochemical testes, by using activated material coated on copper foil (1 $\text{mg}\cdot\text{cm}^{-2}$ of loading mass), a metallic lithium foil and a Celgard 2500 as cathode, anode, and separator, respectively. 1.0 M LiPF_6 in ethylene carbonate (EC)/diethylene carbonate (DEC) ($V/V = 1:1$) was used as the

electrolyte. All the cells were aged overnight prior to the electrochemical measurements. The relative specific capacity was calculated based on the loading mass of active material.

3 RESULTS AND DISCUSSION

3.1 Synthesis and characterization

Layered TiO_2 was used as the template, and it was intercalated by Benzidine between the interlayer. After polymerization and carbonization, three types of CNS@TiO_2 models ($\text{CNS@TiO}_2\text{NS-500}$, $\text{CNS@TiO}_2\text{SNP-600}$, and $\text{CNS@TiO}_2\text{LNP-700}$) were obtained. The typical scheme illustration is displayed in Fig. 1.

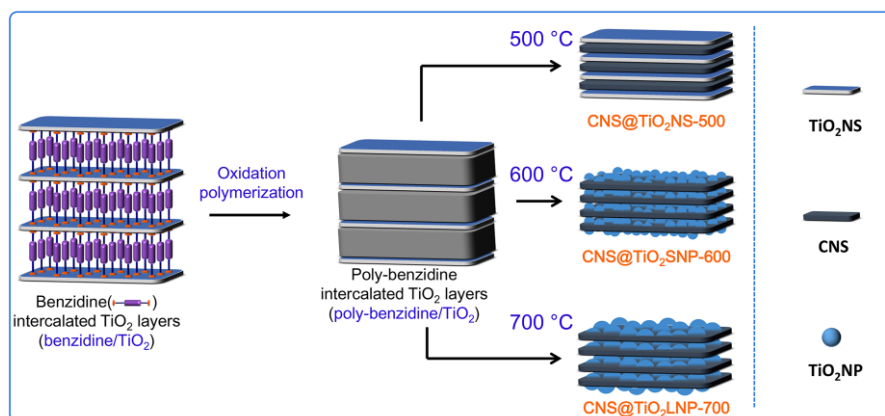


Fig. 1. Scheme illustration of $\text{CNS@TiO}_2\text{NS-500}$, $\text{CNS@TiO}_2\text{SNP-600}$, and $\text{CNS@TiO}_2\text{LNP-700}$

According to the periodic diffraction peak ($0k0$) ($k = 1, 2, 3, \dots$) shown in XRD pattern, the interlayer distance of materials with a typical layered structure can be obtained from the Bragg equation. The XRD pattern of benzylamine intercalated in HTO is exhibited in Fig. 2a. The diffraction characteristic peak located at 9.96° corresponds to the (010) plane of the layered HTO, and the interlayer distance is calculated to be 8.9 \AA . The periodic diffraction peaks shift to a lower angle, and thus the interlayer distance increases. We can conclude that the organic amine has been embedded between the interlayers of HTO. As is known to us, the increased interlayer distance is determined by the type of material

between the layers, and the value is equal to the molecular chain length of benzylamine and benzidine, which was reported in our previous study^[18]. After benzylamine was embedded between HTO layers through an acid-base neutralization reaction, the diffraction period peak of benzylamine/ TiO_2 (010) shifts to a lower angle (Fig. 2a), and the interlayer distance is calculated to be 18.4 \AA . We can find that the increased interlayer distance is twice as long as the molecular chain length of benzylamine (Table 1), indicating that benzylamine interacts with the upper and lower layers of the HTO.

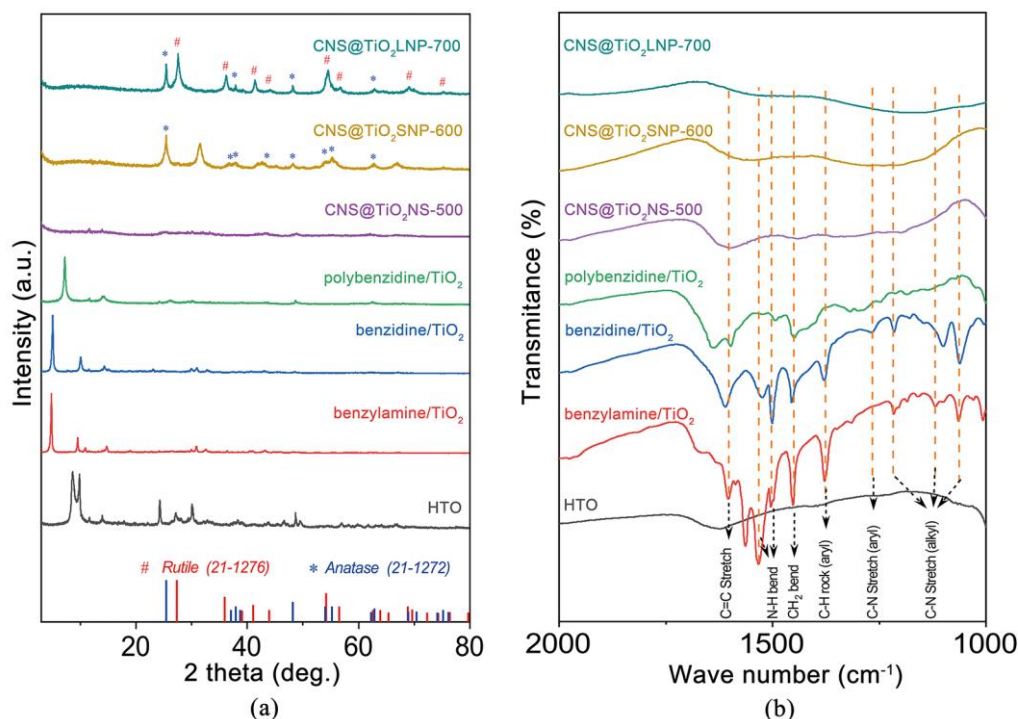


Fig. 2. (a) XRD, (b) FT-IR of the HTO, benzylamine/TiO₂, benzidine/TiO₂, polybenzidine/TiO₂, CNS@TiO₂NS-500, CNS@TiO₂SNP-600, and CNS@TiO₂LNP-700

Benzylamine can be easily embedded between the interlayers of the HTO template. However, it has a low boiling point, and only possesses one amino group that can be connected to the template. When large amounts of benzylamine are utilized as the carbon source, it usually escapes from the reaction system during the carbonization process, and even causes the collapse of the layered HTO template. Benzidine, an organic molecule with two amino groups, shows a high boiling point of 400 °C, and can be carbonized at low temperature^[23]. In this study, benzylamine was embedded into the HTO template through a wedge effect

to increase the interlayer distance of HTO. And then benzidine was successfully embedded between the layers of HTO through an exchange reaction (Fig. 2a). Benzidine, containing additional two amino groups, can interact with the upper and lower layers of the HTO template. Therefore, it can maintain the structural integrity and reduce the loss of carbon source under high-temperature conditions. The interlayer distance of benzidine/TiO₂ is 17.8 Å, and the increased interlayer distance is the length of the chain molecule of benzidine after the exchange reaction (Table 1).

Table 1. Interlayer Distance Calculated from (010) Diffraction Peak from XRD Data

Sample	HTO	Benzylamine/TiO ₂	Benzidine/TiO ₂	Polybenzidine/TiO ₂
2θ(°)	9.96	4.82	5.01	7.24
Interlayer distance (Å)	8.9	18.4	17.8	12.2

Fourier transform infrared spectroscopy (FT-IR) spectrum demonstrates that the typical characteristic peaks (C–N (alkyl)) of benzylamine/TiO₂ appear at 1060, 1116, and 1215 cm⁻¹ (Fig. 2b), indicating the successful intercalation of benzidine into the interlayers of the HTO template after the replacement of benzylamine. A new typical characteristic peak (C–N (aryl)) of benzidine/TiO₂ appears at 1264 cm⁻¹, which demonstrates that benzidine has been successfully embedded into the HTO layers^[24, 25]. In order to reduce the weight loss of benzidine

during high-temperature carbonization process, the benzidine/TiO₂ was put in a tube furnace and pre-polymerized at 200 °C for 3 hours under oxygen atmosphere. And then the polybenzidine/TiO₂ was obtained. Compared with the benzidine/TiO₂, the layered periodic diffraction peaks of polybenzidine/TiO₂ shift to a larger angle (Fig. 2b). It demonstrates that benzidine can partially escape from the lath-shaped HTO layers, resulting in a decrease in the interlayer distance. The morphology of the polybenzi-

dine/TiO₂ maintains the intact structure of the HTO template during the process of intercalation, replacement, and polymerization (Fig. S2a~2c).

There are no obvious periodic diffraction peaks for CNS@TiO₂NS-500 from the XRD spectrum (Fig. 2a). The possible reason is that the small size of the HTO template

shows a weaker force and few restrictions of the organic molecules between the interlayers after carbonization. Therefore, obvious distortion of bonds and increased disorder of the interlayer distance^[23] are easily observed. However, the CNS@TiO₂NS-500 still maintains a regular layered structure as displayed in Fig. 4a.

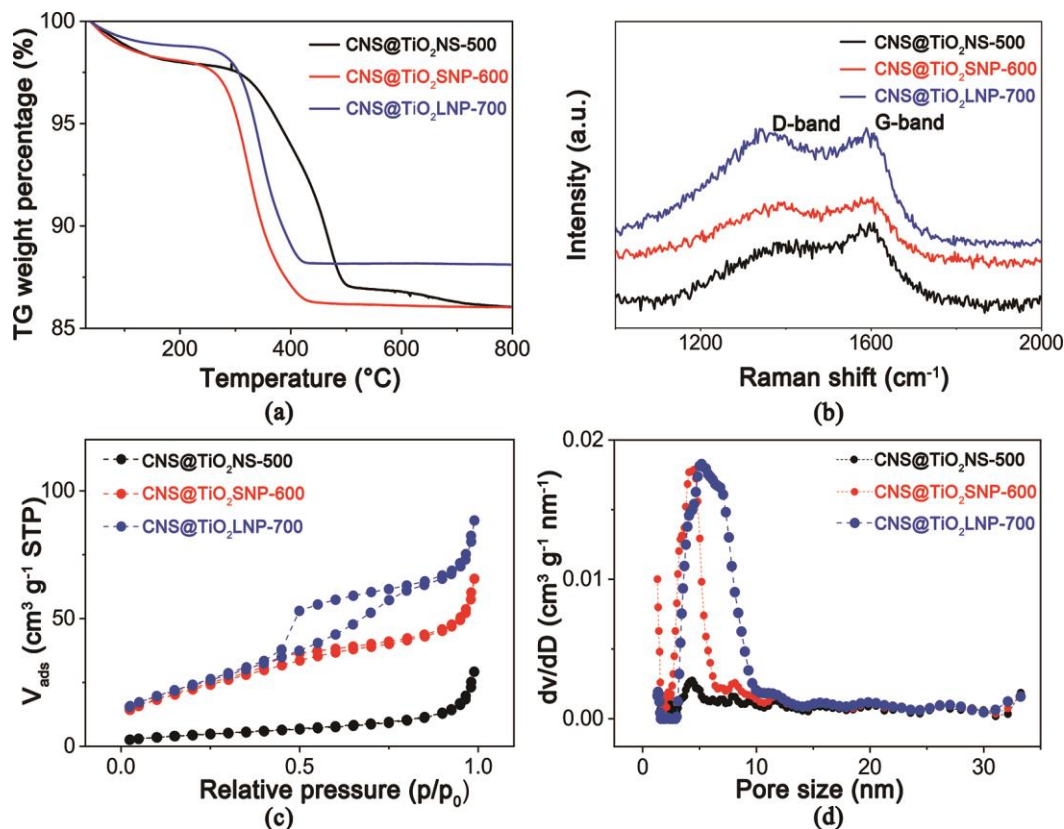


Fig. 3. (a) TG survey, (b) Raman spectra, (c) N₂ adsorption-desorption isotherms, and (d) pore size distribution of the CNS@TiO₂NS-500, CNS@TiO₂SNP-600, and CNS@TiO₂LNP-700

Under the calcination temperature of 600 °C, the crystal structure of TiO₂ undergoes a phase transformation. Diffraction peaks of anatase crystal structure in CNS@TiO₂SNP-600 are obviously observed from the XRD spectrum (Fig. 2a). According to the Scherer's formula, the size of anatase TiO₂ nanoparticles is calculated to be 16.9 nm. Obvious diffraction peaks of both anatase and rutile crystal structure appear in the XRD spectrum of the CNS@TiO₂LNP-700 (Fig. 2a). The size of rutile TiO₂ nanoparticles is calculated to be 57.0 nm. The larger size of TiO₂ nanoparticles tends to restrict the improvement of storage capacity of interfacial lithium ions. Rutile TiO₂ is more stable than anatase TiO₂, and can accommodate < 0.1 mol Li⁺ per TiO₂ unit. The existing rutile TiO₂ tends to further restrict the lithium storage capacity of CNS@TiO₂LNP-700^[26-28]. The FT-IR spectra of polybenzidine/TiO₂ (Fig. 2b) demonstrate that the numbers of

C-H, N-H, and CH₂ vibration peaks are significantly reduced, further confirming that the polymerization reaction is a process of dehydrogenation and deamination. After carbonization at 500, 600, and 700 °C, no vibration absorption peaks of N-H, C-H, and CH₂ appear in the FT-IR spectra of CNS@TiO₂NS-500, CNS@TiO₂SNP-600, and CNS@TiO₂LNP-700. These results indicate that the polybenzidine/TiO₂ has been completely carbonized without obvious change of the layered structure (Fig. S2d~2f). The color of all samples changes from yellow to black after the carbonization treatment (Fig. S2g). As presented in Fig. 3a, carbon contents in CNS@TiO₂NS-500, CNS@TiO₂SNP-600, and CNS@TiO₂LNP-700 are 12.3%, 12.3%, and 10.8%, respectively. A very small difference in carbon content does not bring about a large difference in the electrochemical performance of the corresponding composite materials.

Raman spectra were used to detect carbon structure as shown in Fig. 3b, D peak (carbon atom lattice defects) and G peak (sp^2 bond phonon vibration of carbon atom) appear at 1349 and 1596 cm^{-1} for carbon materials, respectively. The ratio of D and G bands (I_D/I_G) for the CNS@TiO₂NS-500, CNS@TiO₂SNP-600, and CNS@TiO₂LNP-700 is 0.89, 0.95, and 1.02, respectively. With the increasement of calcination temperature, the corresponding CNS@TiO₂NS-500, CNS@TiO₂SNP-600, and CNS@TiO₂LNP-700 exhibits higher degree of disorder in the carbon sheets, which is beneficial to improve the electrical conductivity of TiO₂ in the composite^[29-31].

As shown in Fig. 3c, BET measurement indicates CNS@TiO₂NS-500 shows a small specific surface area ($16.0 \text{ m}^2\cdot\text{g}^{-1}$). However, the CNS@TiO₂SNP-600 displays a larger

specific surface area ($81.0 \text{ m}^2\cdot\text{g}^{-1}$) than the CNS@TiO₂NS-500, which is mainly ascribed to small-sized TiO₂ nanoparticles rather than TiO₂ sheets in CNS@TiO₂NS-500. The CNS@TiO₂LNP-700 displays negligible improvement ($86.4 \text{ m}^2\cdot\text{g}^{-1}$) compared with the CNS@TiO₂SNP-600 ($81.0 \text{ m}^2\cdot\text{g}^{-1}$). The possible reason may be due to the increased interlayer distance of CNS in CNS@TiO₂LNP-700 which is easy to improve the specific surface area, while the increased size of TiO₂ nanoparticles simultaneously tends to decrease the specific surface area of the composite. The pore size distributions of CNS@TiO₂NS-500, CNS@TiO₂SNP-600, and CNS@TiO₂LNP-700 are shown in Fig. 3d, which clearly demonstrates the existence of mesoporous structures (2~50 nm) in all three composites.

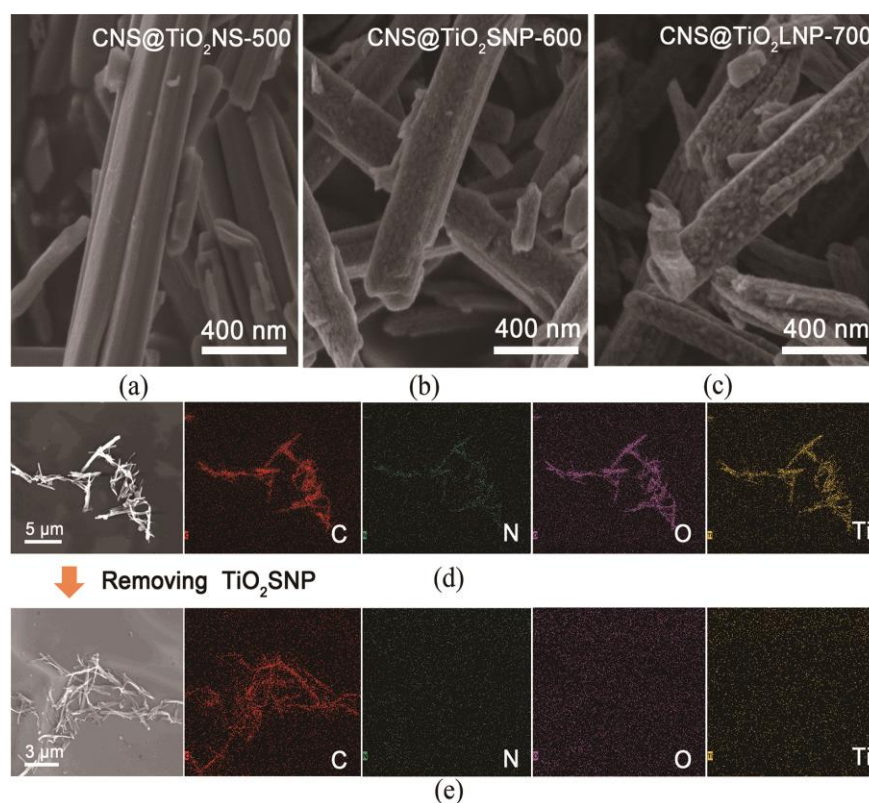


Fig. 4. SEM of (a) CNS@TiO₂NS-500, (b) CNS@TiO₂SNP-600, and (c) CNS@TiO₂LNP-700; (d) SEM and elemental mapping of CNS@TiO₂SNP-600; (e) SEM and elemental mapping of the CNS-600 after removing TiO₂ from the CNS@TiO₂SNP-600

The morphologies of CNS@TiO₂NS-500, CNS@TiO₂SNP-600, and CNS@TiO₂LNP-700 are shown in Fig. 4a~c, respectively. All of them maintain a regular slatted structure and mimic the morphology of the HTO template after carbonization. As shown in Fig. S3, C, N, O, and Ti elements are uniformly distributed in the CNS@TiO₂NS-500. The element mapping results of CNS@TiO₂SNP-600 display the uniform distribution of C, N, O, and Ti elements (Fig. 4d),

which are consistent with the XRD results in Fig. 2a. TiO₂ nanoparticles with larger size can be found in CNS@TiO₂LNP-700 (Fig. 4c), and element mapping results display a uniform distribution of C, N, O, and Ti elements (Fig. S5). To further validate the CNS@TiO₂NS-500, CNS@TiO₂SNP-600, and CNS@TiO₂LNP-700 with layered structures, carbon materials were retained by removing TiO₂ (including anatase and rutile) between the layers via a simple

wet chemical etching method. The element mapping images of carbon nanosheets (CNS-600) are shown in Fig. 4e. It is clear that the distribution of C element is in accordance with the SEM image of CNS-600. The element mapping and EDS results of CNS-500 and CNS-700 are shown in Fig. S6 and Fig. S7, respectively. Similarly, the element of C is in accordance with the SEM images of CNS-500 and CNS-700, respectively. These results indicate that TiO_2 nanoparticles have been completely removed from the $\text{CNS@TiO}_2\text{NS-500}$,

$\text{CNS@TiO}_2\text{SNP-600}$, and $\text{CNS@TiO}_2\text{LNP-700}$. The morphologies of $\text{CNS@TiO}_2\text{NS-500}$, $\text{CNS@TiO}_2\text{SNP-600}$, and $\text{CNS@TiO}_2\text{LNP-700}$ are shown in Fig. S8, the obtained carbon materials present sheet-like structure and stack together after removing TiO_2 , mimicking the morphology of the HTO template. The specific surface area of CNS-500, CNS-600, and CNS-700 is 152.6, 388.8, and 566.8 $\text{m}^2\cdot\text{g}^{-1}$, respectively (Fig. S9).

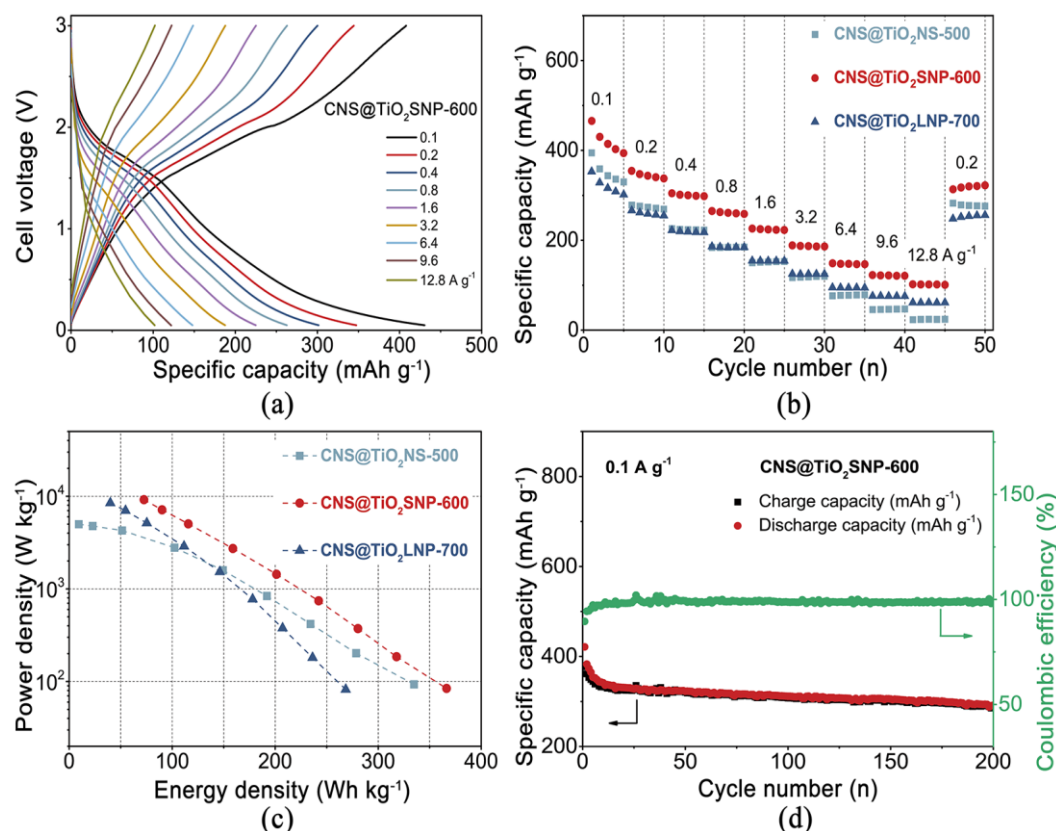


Fig. 5. (a) Representative galvanostatic discharge/charge profiles at various current densities of $\text{CNS@TiO}_2\text{SNP-600}$; (b) Comparison of the rate capability of the $\text{CNS@TiO}_2\text{NS-500}$, $\text{CNS@TiO}_2\text{SNP-600}$, and $\text{CNS@TiO}_2\text{LNP-700}$; (c) Ragone plot of coin cells with $\text{CNS@TiO}_2\text{NS-500}$, $\text{CNS@TiO}_2\text{SNP-600}$, and $\text{CNS@TiO}_2\text{LNP-700}$; (d) Cycling performance of the coin cell with $\text{CNS@TiO}_2\text{SNP-600}$ at $0.1\text{ A}\cdot\text{g}^{-1}$

3.2 Electrochemistry

The constant current charge-discharge tests of the coin cell with $\text{CNS@TiO}_2\text{SNP-600}$ electrode at current density of $0.1\sim 12.8\text{ A}\cdot\text{g}^{-1}$ and voltage windows of $0.05\sim 3\text{ V}$ are shown in Fig. 5a. The charge-discharge curve of $\text{CNS@TiO}_2\text{SNP-600}$ exhibits a steep trend according with a typical capacitive energy storage^[32, 33], which is similar to that of $\text{CNS@TiO}_2\text{NS-500}$ (Fig. S10a) and $\text{CNS@TiO}_2\text{LNP-700}$ (Fig. S11a). The discharge specific capacity at current density of $0.1, 0.2, 0.4, 0.8, 1.6, 3.2, 6.4, 9.6$, and $12.8\text{ A}\cdot\text{g}^{-1}$ is 430.4,

347.3, 301.4, 262.7, 224.9, 187.5, 147.8, 121.9, and $101.8\text{ mAh}\cdot\text{g}^{-1}$, respectively (Fig. 5b). The discharge specific capacities of all three coins are higher than the theoretical specific capacity of TiO_2 , which is mainly ascribed to the special layered structure of carbon nanosheets and anatase TiO_2 nanoparticles^[20, 34, 35]. The discharge specific capacity of $\text{CNS@TiO}_2\text{SNP-600}$ rapidly increases to $322.1\text{ mAh}\cdot\text{g}^{-1}$ when the current density returns back to $0.2\text{ A}\cdot\text{g}^{-1}$, which is higher than that of $\text{CNS@TiO}_2\text{NS-500}$ and $\text{CNS@TiO}_2\text{LNP-700}$. The $\text{CNS@TiO}_2\text{SNP-600}$ displays a better rate performance

than the other two electrodes. Meanwhile, the TiO₂ nanosheets between the CNS layers in CNS@TiO₂SNP-600 are in-situ transformed into anatase nanoparticles (16.9 nm). The small-sized nanoparticles generated by in-situ transformation can provide more interface contact with the interlayered CNS. And thus it contributes to an additional storage capacity of lithium ions^[26]. However, the size of TiO₂ particles in CNS@TiO₂LNP-700 is larger than that in the CNS@TiO₂SNP-600, which tends to reduce the effective contact area between the nanoparticles and the carbon nanosheets. Apparently, the TiO₂ nanoparticles with a large size have limited the capacitance effect of CNS@TiO₂LNP-700. Its discharge specific capacity is 328.2 mAh·g⁻¹ at a current density of 0.1 A·g⁻¹. Usually, the discharge specific capacity of materials is highly influenced by their conductivity^[36, 37]. The conductivity of CNS@TiO₂NS-500 (6.18×10^{-5} s·cm⁻¹) is lower than that of CNS@TiO₂LNP-700 (2.36×10^{-1} s·cm⁻¹). Therefore, the discharge specific capacity of CNS@TiO₂NS-500 decreases significantly than that of CNS@TiO₂LNP-700. The discharge specific capacity of CNS@TiO₂NS-500 (23.2 mAh·g⁻¹) is obviously lower than that of the CNS@TiO₂LNP-700 (61.1 mAh·g⁻¹) at a current density of 12.8 A·g⁻¹. However, the conductivity of CNS@TiO₂SNP-600 (1.90×10^{-2} s·cm⁻¹) is slightly lower than that of CNS@TiO₂LNP-700 (2.36×10^{-1} s·cm⁻¹). The difference in conductivity does not lead to a significant difference in the electrochemical performance of CNS@TiO₂SNP-600 and CNS@TiO₂LNP-700 (Fig. 5b). Fig. 5c shows specific energy density and specific power density of the coin cells with the CNS@TiO₂NS-500, CNS@TiO₂SNP-600, and CNS@TiO₂LNP-700. The coin cell with CNS@TiO₂SNP-600 generates a specific energy density of 366.3 Wh·kg⁻¹ and a specific power density of 84.2 W·kg⁻¹ at 0.1 A·g⁻¹. A specific energy density of 72.5 Wh·kg⁻¹ and a specific power of 9.1 kW·kg⁻¹ still remains at a high current density of 12.8 A·g⁻¹. The CNS@TiO₂SNP-600 exhibits higher specific energy density and specific power density than that of CNS@TiO₂NS-500 and CNS@TiO₂LNP-700.

In addition to show ultra-high specific capacity and rate performance, CNS@TiO₂SNP-600 also exhibits excellent cycling stability properties. Fig. 5d illustrates the cycle stability of the coin cell with CNS@TiO₂NS-500, CNS@TiO₂SNP-600, and CNS@TiO₂LNP-700 electrode during the charge-discharge process in lithium-ion battery. The coin cell is charged and discharged for 200 cycles at a current density of 0.1 A·g⁻¹ and at a voltage window of 0.05~3 V. The charge-discharge behavior of the first 6 cycles is the activation process of the material. A solid electrolyte interface (SEI) layer is easily formed on the surface of the active material during the charge-discharge process^[38, 39]. Although the SEI layer can deplete both Li and electrolyte, the passivation layer can maintain the stability of the material. The specific discharge capacity of CNS@TiO₂SNP-600 stabilizes at 354 mAh·g⁻¹ after 6 cycles, which is ascribed to the inevitable formation of SEI layers. The specific discharge capacity is 312 mAh·g⁻¹ after 100 cycles, and the relative capacity retention rate is 88.1%. After 200 cycles, the discharge specific capacity is 294 mAh·g⁻¹ and the capacity retention still remains 83.1%, demonstrating a remarkable cycling stability for CNS@TiO₂SNP-600.

The diffusion kinetics of lithium ions in CNS@TiO₂NS-500, CNS@TiO₂SNP-600, and CNS@TiO₂LNP-700 electrodes were further investigated by cyclic voltammetry tests, as shown in Figs. 6 and S12. A pair of wide reduction-oxidation peaks appear in the voltage windows from 1.0 to 2.5 V as shown in Fig. 6a for CNS@TiO₂SNP-600, which corresponds to the embedding of lithium ions in the crystal structure of TiO₂. The quasi rectangular wave of CNS@TiO₂SNP-600 is similar to that of the CNS@TiO₂NS-500 (Fig. S10b) and CNS@TiO₂LNP-700 (Fig. S11b), typical oxidation and reduction peaks appear at 2.10 and 1.70 V, 2.10 and 1.74 V, respectively. It demonstrates that the three electrodes possess the ability of capacitive energy storage^[32, 40-43]. These results are in accordance with the exfoliation/embedding of lithium ions in TiO₂^[44, 45].

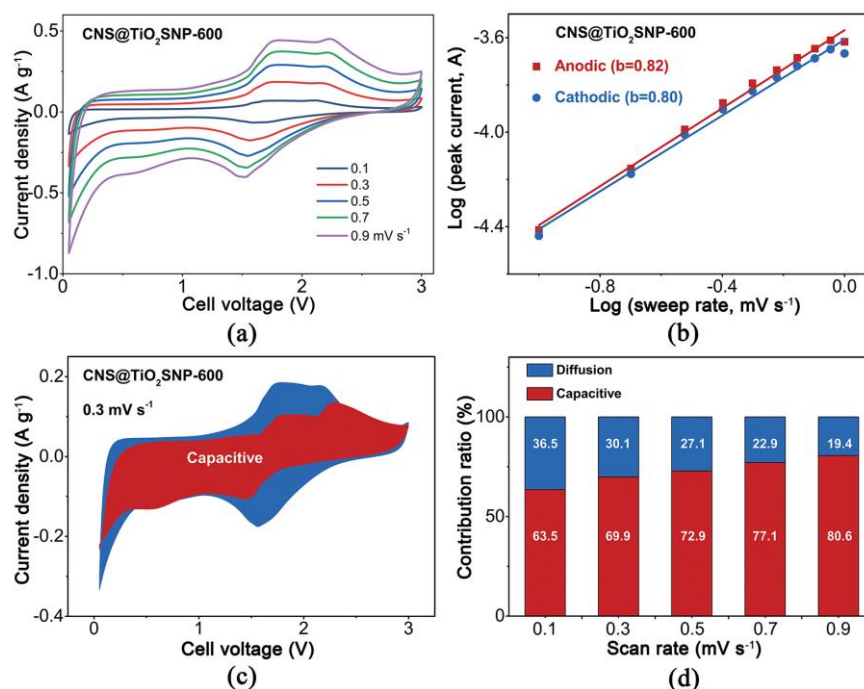


Fig. 6. (a) Cyclic voltammetric curve of CNS@TiO₂SNP-600. (b) b-value calculated by the relationship between the scan rate and the peak current. (c) Segregation of capacitive and diffusion-controlled currents in CNS@TiO₂SNP-600 at a scan rate of 0.3 mV·s⁻¹. (d) Contribution ratio of capacitance and diffusion-controlled current at various scan rates

To further understand the mechanism of lithium storage, we have conducted a kinetic analysis according to the report by Dunn et al.^[46]. The relationship between peak current (i) and scanning rates (ν) is shown in the following formula: $i = a\nu^b$. Here, a and b are adjustable values. Based on the slope of $\log(i) - \log(\nu)$, when the calculated value of b is close to 0.5 and 1.0, the corresponding current is mainly controlled by the diffusion and surface capacitance, respectively. b value of CNS@TiO₂SNP-600 during the charge and discharge process is calculated to be 0.82 and 0.80, respectively (Fig. 6b), demonstrating that the capacitance current is dominant^[47]. The redox reaction occurs on the surface of the small-sized TiO₂ nanoparticles between the interlayers of the CNS@TiO₂SNP-600, which can effectively reduce the excessive insertion energy storage occurring inside the interlayers due to the large sized TiO₂ (Figs. S12a and S12b). In contrast, the large size of TiO₂ nanoparticles in CNS@TiO₂LNP-700 can prolong the distance of lithium ion transport and impede the diffusion kinetics (The b -value of CNS@TiO₂SNP-600 nanosheet composites was significantly higher than that of CNS@TiO₂LNP-700, as shown in Figs. S12b and 6b). In addition, a microscopic structure of electric double layer was found. Both the high conductivity of carbon nanosheets and the close contact between the layers and small-sized TiO₂

nanoparticles contribute to a higher specific capacity than the theoretical specific capacity. The discharge specific capacity achieves to 101.8 mAh·g⁻¹ at a high current density of 12.8 A·g⁻¹. In comparison, an amount of redox reaction occurs on the surface of TiO₂ between the interlayers of CNS@TiO₂NS-500 and CNS@TiO₂LNP-700 (Figs. S12a and S12b), but its rate performance was severely limited by the low electronic conductivity. The ratios of the pseudo-capacitance contribution of the three composites at different scan rates are calculated from the relationship of $i = k_1\nu + k_2\nu^{1/2}$. Here, $k_1\nu$ and $k_2\nu^{1/2}$ denote the capacitance and diffusion currents, respectively. The pseudo-capacitive contribution for CNS@TiO₂SNP-600 electrode is as high as 69.9% at a scan rate of 0.3 mV·s⁻¹ (Fig. 6c). It can be seen that the diffusion-controlled currents mainly occur near the cathode/anode peaks, which are associated with the redox reaction of lithium ion insertion/de-insertion. The ratio of pseudo-capacitive storage capacity contribution increases gradually with the increasing scan rate and achieves to 80.6% at a scan rate of 0.9 mV·s⁻¹ (Fig. 6d). The pseudo-capacitive contribution of CNS@TiO₂NS-500 and CNS@TiO₂LNP-700 electrodes at different scan rates is shown in Figs. S12e and S12f, respectively.

4 CONCLUSION

The two-dimensional composite materials composed of TiO₂ and carbon nanosheets was successfully synthesized via high-temperature polymerization and carbonization method by using the layered HTO as template. Specifically, benzylamine was embedded through the wedge effect to increase the interlayer distance, and then benzidine was inserted between the HTO layers as a carbon source through an exchange reaction. The morphology and size of TiO₂ were easily influenced by the carbonization temperature. TiO₂ nanosheets (TiO₂NS), TiO₂ small-sized nanoparticles (TiO₂SNP), and TiO₂ large-sized nanoparticles (TiO₂LNP) inserted between the carbon nanosheets (CNS) were obtained

under three different heat-treatment temperature of 500, 600, and 700 °C, respectively. The CNS@TiO₂SNP-600 displays a high specific discharge capacity of 430.4 mAh·g⁻¹ at a current density of 0.1 A·g⁻¹, and the capacity retention rate is 88.1% after 100 cycles. A high specific discharge capacity of 101.8 mAh·g⁻¹ still remains at a high current density of 12.8 A·g⁻¹. These results indicate the capacitance effect, originating from the close contact between CNS and TiO₂SNP, can greatly increase the storage capacity of lithium ions; and the CNS grown in situ can improve the rate performance and cycle stability of TiO₂. This kind of materials can be used in the lithium-ion batteries and in other related electrochemical storage and conversion devices.

REFERENCES

- (1) Zhao, Y.; Wang, L. P.; Sougrati, M. T.; Feng, Z. X.; Leconte, Y.; Fisher, A.; Srinivasan, M.; Xu, Z. C. A review on design strategies for carbon based metal oxides and sulfides nanocomposites for high performance Li and Na ion battery anodes. *Adv. Energy Mater.* **2017**, 7, 1601424–70.
- (2) Subramanian, V.; Karki, A.; Gnanasekar, K. I.; Eddy, F. P.; Rambabu, B. Nanocrystalline TiO₂ (anatase) for Li-ion batteries. *J. Power Sources* **2006**, 159, 186–192.
- (3) An, G. H.; Ahn, H. J. Carbon nanofiber/cobalt oxide nanopyramid core-shell nanowires for high-performance lithium-ion batteries. *J. Power Sources* **2014**, 272, 828–836.
- (4) Cho, J. S.; Hong, Y. J.; Kang, Y. C. Design and synthesis of bubble-nanorod-structured Fe₂O₃-carbon nanofibers as advanced anode material for Li-ion batteries. *ACS Nano* **2015**, 9, 4026–4035.
- (5) Yan, C. S.; Chen, G.; Zhou, X.; Sun, J. X.; Lv, C. Template-based engineering of carbon-doped Co₃O₄ hollow nanofibers as anode materials for lithium-ion batteries. *Adv. Funct. Mater.* **2016**, 26, 1428–1436.
- (6) Wang, H. W.; Jia, G. C.; Guo, Y. Y.; Zhang, Y. Q.; Geng, H. B.; Xu, J.; Mai, W. J.; Yan, Q. Y.; Fan, H. J. Atomic layer deposition of amorphous TiO₂ on carbon nanotube networks and their superior Li and Na ion storage properties. *Adv. Mater. Interfaces* **2016**, 3, 1600375–9.
- (7) Wang, X. Y.; Fan, L.; Gong, D. C.; Zhu, J.; Zhang, Q. F.; Lu, B. G. Core-shell Ge@Graphene@TiO₂ nanofibers as a high-capacity and cycle-stable anode for lithium and sodium ion battery. *Adv. Funct. Mater.* **2016**, 26, 1104–1111.
- (8) Etacheri, V.; Yourey, J. E.; Bartlett, B. M. Chemically bonded TiO₂-bronze nanosheet/reduced graphene oxide hybrid for high-power lithium ion batteries. *ACS Nano* **2014**, 8, 1491–1499.
- (9) Hu, T.; Sun, X.; Sun, H. T.; Yu, M. P.; Lu, F. Y.; Liu, C. S.; Lian, J. Flexible free-standing graphene-TiO₂ hybrid paper for use as lithium ion battery anode materials. *Carbon* **2013**, 51, 322–326.
- (10) Kim, H. K.; Mhamane, D.; Kim, M. S.; Roh, H. K.; Aravindan, V.; Madhavi, S.; Roh, K. C.; Kim, K. B. TiO₂-reduced graphene oxide nanocomposites by microwave-assisted forced hydrolysis as excellent insertion anode for Li-ion battery and capacitor. *J. Power Sources* **2016**, 327, 171–177.
- (11) Li, W.; Wang, F.; Liu, Y. P.; Wang, J. X.; Yang, J. P.; Zhang, L. J.; Elzatahry, A. A.; Al-Dahyan, D.; Xia, Y. Y.; Zhao, D. Y. General strategy to synthesize uniform mesoporous TiO₂/graphene/mesoporous TiO₂ sandwich-like nanosheets for highly reversible lithium storage. *Nano Lett.* **2015**, 15, 2186–2193.
- (12) Mo, R. W.; Lei, Z. Y.; Sun, K. N.; Rooney, D. Facile synthesis of anatase TiO₂ quantum-dot/graphene-nanosheet composites with enhanced electrochemical performance for lithium-ion batteries. *Adv. Mater.* **2014**, 26, 2084–2088.
- (13) Qiu, B. C.; Xing, M. Y.; Zhang, J. L. Mesoporous TiO₂ nanocrystals grown in situ on graphene aerogels for high photocatalysis and lithium-ion batteries. *J. Am. Chem. Soc.* **2014**, 136, 5852–5855.
- (14) Ren, G. F.; Hoque, M. N. F.; Liu, J. W.; Warzywoda, J.; Fan, Z. Y. Perpendicular edge oriented graphene foam supporting orthogonal TiO₂ (B) nanosheets as freestanding electrode for lithium ion battery. *J. Am. Chem. Soc.* **2016**, 21, 162–171.

- (15) Ren, Y.; Liu, Z.; Pourpoint, F.; Armstrong, A. R.; Grey, C. P.; Bruce, P. G. Nanoparticulate TiO₂ (B): an anode for lithium-ion batteries. *Angew. Chem. Int. Ed.* **2012**, 124, 2206–2209.
- (16) Wang, D. H.; Choi, D.; Li, J.; Yang, Z. G.; Nie, Z. M.; Kou, R.; Hu, D. H.; Wang, C. M.; Saraf, L. V.; Zhang, J. G. Self-assembled TiO₂-graphene hybrid nanostructures for enhanced Li-ion insertion. *ACS Nano* **2009**, 3, 907–914.
- (17) Fu, W. W.; Li, Y. T.; Chen, M. S.; Hu, Y. J.; Liu, B. H.; Zhang, K.; Zhan, C. Y.; Zhang, M.; Shen, Z. R. An orderly arrangement of layered carbon nanosheet/TiO₂ nanosheet stack with superior artificially interfacial lithium pseudocapacity. *J. Power Sources* **2020**, 468, 228363–7.
- (18) Hu, Y. J.; Li, Y. T.; Cheng, J. F.; Chen, M. S.; Fu, W. W.; Liu, B. H.; Zhang, M.; Shen, Z. R. Intercalation of carbon nanosheet into layered TiO₂ grain for highly interfacial lithium storage. *ACS Appl. Mater. Inter.* **2020**, 12, 21709–21719.
- (19) Li, Y. T.; Chen, M. S.; Cheng, J. F.; Fu, W. W.; Hu, Y. J.; Liu, B. H.; Zhang, M.; Shen, Z. R. Two-dimensional layered ultrathin carbon/TiO₂ nanosheet composites for superior pseudocapacitive lithium storage. *Langmuir* **2020**, 36, 2255–2263.
- (20) Brezesinski, T.; Wang, J.; Polleux, J.; Dunn, B.; Tolbert, S. H. Templated nanocrystal-based porous TiO₂ films for next-generation electrochemical capacitors. *J. Am. Chem. Soc.* **2009**, 131, 1802–1809.
- (21) Mirhashemihaghighi, S.; León, B.; Pérez Vicente, C.; Tirado, J. L.; Stoyanova, R.; Yoncheva, M.; Zhecheva, E.; Sáez Puche, R.; Arroyo, E. M.; Romero de Paz, J. Lithium storage mechanisms and effect of partial cobalt substitution in manganese carbonate electrodes. *Inorg. Chem.* **2012**, 51, 5554–5560.
- (22) Sasaki, T.; Kooli, F.; Iida, M.; Michiue, Y.; Takenouchi, S.; Yajima, Y.; Izumi, F.; Chakoumakos, B. C.; Watanabe, M. A mixed alkali metal titanate with the lepidocrocite-like layered structure. Preparation, crystal structure, protonic form, and acid-base intercalation properties. *Chem. Mater.* **1998**, 10, 4123–4128.
- (23) Ding, W.; Wei, Z. D.; Chen, S. G.; Qi, X. Q.; Yang, T.; Hu, J. S.; Wang, D.; Wan, L. J.; Alvi, S. F.; Li, L. Space-confinement-induced synthesis of pyridinic- and pyrrolic-nitrogen-doped graphene for the catalysis of oxygen reduction. *Angew. Chem. Int. Ed.* **2013**, 125, 11971–11975.
- (24) Akalin, E.; Akyüz, S. Structure and vibrational spectra of benzidine. *J. Mol. Struct.* **2003**, 651, 571–577.
- (25) Akyüz, S.; Bulat, T.; Özel, A. E.; Basar, G. FT-IR and laser Raman spectroscopic investigation of transition metal halide complexes of benzidine. *Vib. Spectrosc.* **1997**, 14, 151–154.
- (26) Wang, J.; Polleux, J.; Lim, J.; Dunn, B. Pseudocapacitive contributions to electrochemical energy storage in TiO₂ (anatase) nanoparticles. *J. Phys. Chem. C* **2007**, 111, 14925–14931.
- (27) Yang, Z. G.; Choi, D.; Kerisit, S.; Rosso, K. M.; Wang, D. H.; Zhang, J.; Graff, G.; Liu, J. Nanostructures and lithium electrochemical reactivity of lithium titanates and titanium oxides: a review. *J. Power Sources* **2009**, 192, 588–598.
- (28) Wu, Q. L.; Xu, J. G.; Yang, X. F.; Lu, F. Q.; He, S. M.; Yang, J. L.; Fan, H. J.; Wu, M. M. Ultrathin anatase TiO₂ nanosheets embedded with TiO₂-B nanodomains for lithium-ion storage: capacity enhancement by phase boundaries. *Adv. Energy Mater.* **2015**, 5, 1401756–9.
- (29) Liu, G. Y.; Zhao, Y. Y.; Tang, Y. F.; Liu, X. D.; Liu, M.; Wu, P. J. In situ sol-gel synthesis of Ti₂Nb₁₀O₂₉/C nanoparticles with enhanced pseudocapacitive contribution for a high-rate lithium-ion battery. *Rare Metals* **2020**, 39, 1063–1071.
- (30) Luo, R.; Ma, Y. T.; Qu, W. J.; Qian, J.; Li, L.; Wu, F.; Chen, R. J. High pseudocapacitance boosts ultrafast, high-capacity sodium storage of 3D graphene foam encapsulated TiO₂ architecture. *ACS Appl. Mater. Inter.* **2020**, 12, 23939–23950.
- (31) Wang, Y. X.; Yang, J. P.; Chou, S. L.; Liu, H. K.; Zhang, W. X.; Zhao, D. Y.; Dou, S. X. Uniform yolk-shell iron sulfide-carbon nanospheres for superior sodium-iron sulfide batteries. *Nat. Commun.* **2015**, 6, 1–9.
- (32) Augustyn, V.; Come, J.; Lowe, M. A.; Kim, J. W.; Taberna, P. L.; Tolbert, S. H.; Abruña, H. D.; Simon, P.; Dunn, B. High-rate electrochemical energy storage through Li⁺ intercalation pseudocapacitance. *Nat Mater.* **2013**, 12, 518–522.
- (33) Augustyn, V.; Simon, P.; Dunn, B. Pseudocapacitive oxide materials for high-rate electrochemical energy storage. *Energy Environ. Sci.* **2014**, 7, 1597–1614.
- (34) Li, D. D.; Zhang, L.; Chen, H. B.; Wang, J.; Ding, L. X.; Wang, S. Q.; Ashman, P. J.; Wang, H. H. Graphene-based nitrogen-doped carbon sandwich nanosheets: a new capacitive process controlled anode material for high-performance sodium-ion batteries. *J. Mater. Chem. A* **2016**, 4, 8630–8635.
- (35) Li, S.; Qiu, J. X.; Lai, C.; Ling, M.; Zhao, H. J.; Zhang, S. Q. Surface capacitive contributions: towards high rate anode materials for sodium ion batteries. *Nano Energy* **2015**, 12, 224–230.
- (36) Zhang, M.; Hu, Y. J.; Cheng, J. F.; Fu, W. W.; Shen, Z. R. Synthesis of highly-ordered two-dimensional hierarchically porous carbon nanosheet stacks as advanced electrode materials for lithium-ion storage. *ACS Appl. Energy Mater.* **2020**, 4, 226–232.
- (37) Chen, Y. N.; Fu, K.; Zhu, S. Z.; Luo, W.; Wang, Y. B.; Li, Y. J.; Hitz, E.; Yao, Y. G.; Dai, J. Q.; Wan, J. Y.; Danner, V. A.; Li, T.; Hu, L. B. Reduced

- graphene oxide films with ultrahigh conductivity as Li-ion battery current collectors. *Nano Lett.* **2016**, 16, 3616–3623.
- (38) Ventosa, E.; Madej, E.; Zampardi, G.; Mei, B.; Weide, P.; Antoni, H.; Mantia, F. L.; Muhler, M.; Schuhmann, W. Solid electrolyte interphase (SEI) at TiO₂ electrodes in Li-ion batteries: defining apparent and effective SEI based on evidence from X-ray photoemission spectroscopy and scanning electrochemical microscopy. *ACS Appl. Mater. Inter.* **2017**, 9, 3123–3130.
- (39) Ren, H.; Yu, R. B.; Qi, J.; Zhang, L. J.; Jin, Q.; Wang, D. Hollow multishelled heterostructured anatase/TiO₂ (B) with superior rate capability and cycling performance. *Adv. Mater.* **2019**, 31, 1805754–7.
- (40) Hao, B.; Yan, Y.; Wang, X. B.; Chen, G. Synthesis of anatase TiO₂ nanosheets with enhanced pseudocapacitive contribution for fast lithium storage. *ACS Appl. Mater. Inter.* **2013**, 5, 6285–6291.
- (41) Lou, S. F.; Zhao, Y.; Wang, J. J.; Yin, G. P.; Du, C. Y.; Sun, X. L. Ti-based oxide anode materials for advanced electrochemical energy storage: lithium/sodium ion batteries and hybrid pseudocapacitors. *Small* **2019**, 15, 1904740–44.
- (42) Muller, G. A.; Cook, J. B.; Kim, H. S.; Tolbert, S. H.; Dunn, B. High performance pseudocapacitor based on 2D layered metal chalcogenide nanocrystals. *Nano Lett.* **2015**, 15, 1911–1917.
- (43) Que, L. F.; Yu, F. D.; Wang, Z. B.; Gu, D. M. Pseudocapacitance of TiO_{2-x}/CNT anodes for high-performance quasi-solid-state Li-ion and Na-ion capacitors. *Small* **2018**, 14, 1704508–9.
- (44) Wei, H.; Rodriguez, E. F.; Hollenkamp, A. F.; Bhatt, A. I.; Chen, D. H.; Caruso, R. A. High reversible pseudocapacity in mesoporous yolk-shell anatase TiO₂/TiO₂ (B) microspheres used as anodes for Li-ion batteries. *Adv. Funct. Mater.* **2017**, 27, 1703270–9.
- (45) Xing, Y. L.; Wang, S. B.; Fang, B. Z.; Song, G.; Wilkinson, D. P.; Zhang, S. C. N-doped hollow urchin-like anatase TiO₂@C composite as a novel anode for Li-ion batteries. *J. Power Sources* **2018**, 385, 10–17.
- (46) Augustyn, V.; Come, J.; Lowe, M. A.; Kim, J. W.; Taberna, P.; Tolbert, S. H.; Abruña, H. D.; Simon, P.; Dunn, B. High-rate electrochemical energy storage through Li⁺ intercalation pseudocapacitance. *Nat. Mater.* **2013**, 12, 518–522.
- (47) Jiang, J. M.; Zhang, Y. D.; An, Y. F.; Wu, L. Y.; Zhu, Q.; Dou, H.; Zhang, X. G. Engineering ultrathin MoS₂ nanosheets anchored on N-Doped carbon microspheres with pseudocapacitive properties for high-performance lithium-ion capacitors. *Small. Methods* **2019**, 7, 1900081–10.